ESTIMATION AND UPDATING OF DIGITAL SURFACE MODEL (DSM) USING WORLDVIEW-3 DATASET

Indra Bahadur Chhetri[1] and Junichi Susaki[2]

[1]Department of Civil and Earth Resources Engineering, Graduate School of Engineering, Kyoto University, Japan,
Email: indra.chhetri.63z@st.kyoto-u.ac.jp

[2]Dapartment of Urban Management, Graduate School of Engineering, Kyoto University, Japan
Email: susaki.junichi.3r@kyoto-u.ac.jp

KEY WORDS: WorldView-3, Image matching, RPC model, 3D coordinates, DSM

ABSTRACT

Very high-resolution satellite sensor is delivered with rational polynomial coefficients (RPC) as an alternative representation of the sensor model. The use of these rational polynomial coefficients has become one of the standards for very high-resolution satellite imagery (VHRSI) for the production of relevant spatial data. The RPC model is used in determining spatial data for all features in the captured satellite image. This paper aims to evaluate the accuracy of a digital surface model (DSM) generated by processing Ortho-Ready Standard imagery from WorldView-3 using supplied RPCs. The method consists of a basic photogrammetry approach to solve four residual equations composed of stereo pairs via the RPC model. In our experiment, image pixel matching was performed based on homography transformation stereo matching in conjunction with normalized cross-correlation coefficient in identifying dense corresponding tie-points between the images. These dense point correspondences generated were then used to determine the three-dimensional coordinates by employing the RPC model. To perform the accuracy test, the three dimensional (3D) coordinates estimated at points of interest using 49 ground control points (GCPs) were evaluated for the image acquired over Thimphu, Bhutan on 27th August 2020. The average root-mean-square errors (RMSEs) of easting, northing and height evaluated for the coordinates estimated from stereo images were 2.90 m, 2.92 m and 1.64 m respectively. The result is based on a bias-corrected RPC model with two shift parameters using one reliable GCP. Additionally, visual comparisons of interpolated surfaces generated using Inverse Distance Weighted and Kriging interpolation mechanisms have been compared. The findings highlight that the proposed method is simple and effective in determining 3D coordinates at points of interest that have the potential to generate explicit image-based 3D information resulting in a reasonable approximation.

1. INTRODUCTION

Digital elevation models (DEMs) and digital surface models (DSMs) are the generally adopted data structures for storing geo-spatial datasets used for geographical information analysis. The distinction between them may apply as: a DSM is an elevation model that includes the top of everything, including buildings, tree tops, and ground where there is nothing else on top of it, whereas a DEM is a bare land surface model, in which trees, buildings or other non-ground objects are virtually removed. Digital Terrain Model (DTM) by then is a more generic term referring to a DEM with one or more types of terrain information. When dealing with only one terrain information type (i.e., height), this is a DEM i.e. DEM is a subset of DTM (Štular et al., 2021). DSMs or DEMs are widely used in surveying and mapping, land use and planning, environmental assessment, disaster relief, civil engineering, mining, agriculture, and updating existing maps. In order to cater to these applications, they should be up to date. A fast and economic production mechanism is demanded. Moreover, the last but the most important quality in their production is the demand for greater 3D accuracy in order to guarantee data sets free of errors and outliers.
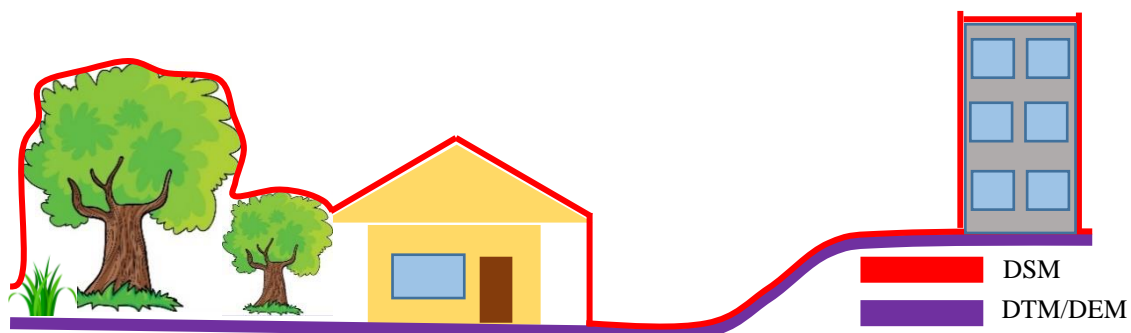

Figure 1: Schematic diagram showing difference between DSM, DEM and DTM

There are various sensors/techniques available for generation of elevation data: airborne light detection and ranging (LiDAR), aerial photogrammetry and optical and space borne sensors (Fratarcangeli et al., 2016). The first global dataset by Shuttle Radar Topography Mission (SRTM) has (90 m) pixel spacing with absolute and relative height accuracies of 9 m and 10 m respectively was based on a spaceborne radar instrument (Takaku et al., 2014). Elevation data, Advanced Spaceborne Thermal Emission and Reflectance Radiometer Global Digital Elevation Model (ASTER/GDEM) from ASTER instrument on-board NASA's Terra satellite was obtained using optical technique, has the height accuracy of 13 m in (30 m) pixel spacing (Hengl & Reuter, 2011; Takaku et al., 2014). However, spatial characteristics of these data show a relatively higher absolute height error with low spatial resolution (Rodríguez et al., 2006). Comparatively, airborne light detection and ranging (LiDAR) data gives more accurate DSMs within ± 15 cm, however it is not economical and has limited area coverage than satellite based imagery (Susaki & Kishimoto, 2015).

Presently, very-high resolution (less than 1 m) satellite sensors allow the acquisition of spatial data directly which are equivalent to DSM. For example, the triplet imagery from Advanced Land Observing Satellite-Panchromatic Remote-sensing Instrument for Stereo Mapping (ALOS-PRISM) was used to generate elevation data satisfying height accuracy within 5 m RMSEs (Takaku et al., 2014). Additionally, Susaki & Kishimoto (2015) examined the accuracies of DSM generated by using multi-temporal triplet images from ALOS-PRISM. Their experimental results showed that the average planimetric and height RMSEs were 3.26 m and 2.71 m respectively. In this respect, the availability of new high-resolution optical spaceborne sensors offers new potential for DSMs generation. Among all these advantages, low cost (in comparison to aerial imagery of small areas included into one scene is concerned), speed of data acquisition and processing and relaxed logistics arrangements are quite important factors to be considered for areas where the organization of aerial flights can be difficult. Therefore, taking advantage of the capability of optical imagery in generating greater accurate DSMs, this study aims to evaluate the accuracy of the three-dimensional (3D) coordinates estimated using WorldView-3 (WV-3) data for DSM generation. The remainder of this paper is organized as follows: Section 2 briefly introduces the data used followed by explanation of the proposed methodology in section 3; Section 4 and 5 focuses on presenting experimental results and demonstrates the performance of our method; Section 6 finally provides the concluding remarks together with suggestions for future work.

2. DATASET DESCRIPTION

The bias-compensated RPC model of an Ortho-Ready Standard WV-3 image with supplied RPCs provided by DigitalGlobe acquired over Thimphu, Bhutan on 27th August 2020 was used in our experiment. Table 1 shows the detailed technical characteristics of the WV-3 images used in the study.

Table 1: The technical characteristics of the WV-3 images used

Parameters	WV-3 First Scene	WV-3 Second Scene	Parameters	WV-3 First Scene	WV-3 Second Scene
Product Level	LV2A	LV2A	Mean Sat El	55.6	78.6
Scan Direction	Forward	Forward	Mean in Track View Angle	28.8	-0.4
First Line Time	04:46:19.849859	04:47:10.700114	Mean Cross Track View Angle	12.0	10.3
Mean Sun Az	130.3 (degree)	130.7 (degree)	Mean Off Nadir View Angle	31.0	10.3
Mean Sun El	64.9	65.1	Cloud Cover	0.013	0.006
Mean Sat Az	29.0	101.4	Product GSD	0.40 m	0.40 m

3. METHODOLOGY

3.1 DSM Generation

In our study the DSM generation process consists of four main steps: image matching, 3D ground coordinates estimation from the RPC model, spatial interpolation and accuracy assessment. Figure 2 depicts the overall flow chart of the main steps for DSM generation.

Image matching is one of the most important parts of procedures in DSM generation. It is the process of measuring conjugate points in two or more images (Wang et al., 2020). Here, in the nadir image we search the corresponding image points in the forward image. Figure 3 illustrates the flowchart of the proposed dense point correspondence

generation algorithm. The two input images such that the nadir image is used as a reference image while the forward image acts as the search image.
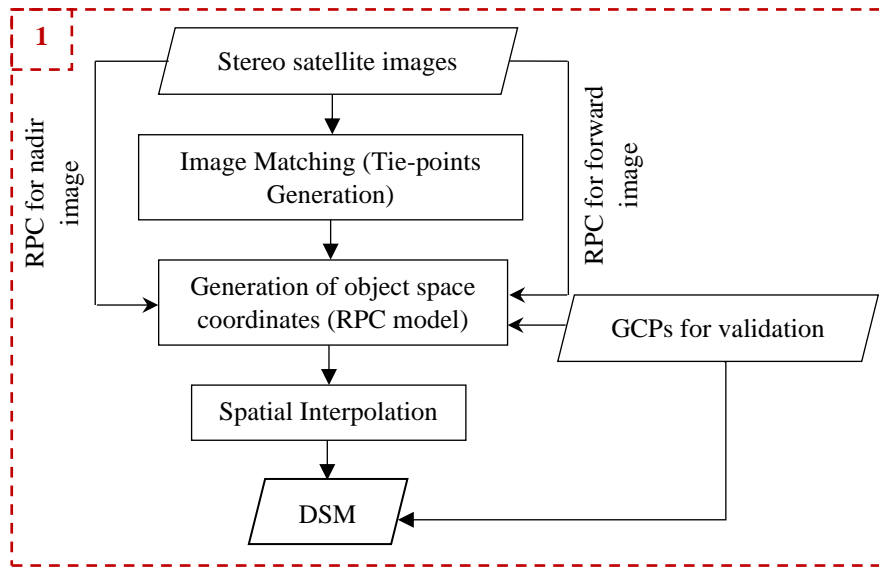

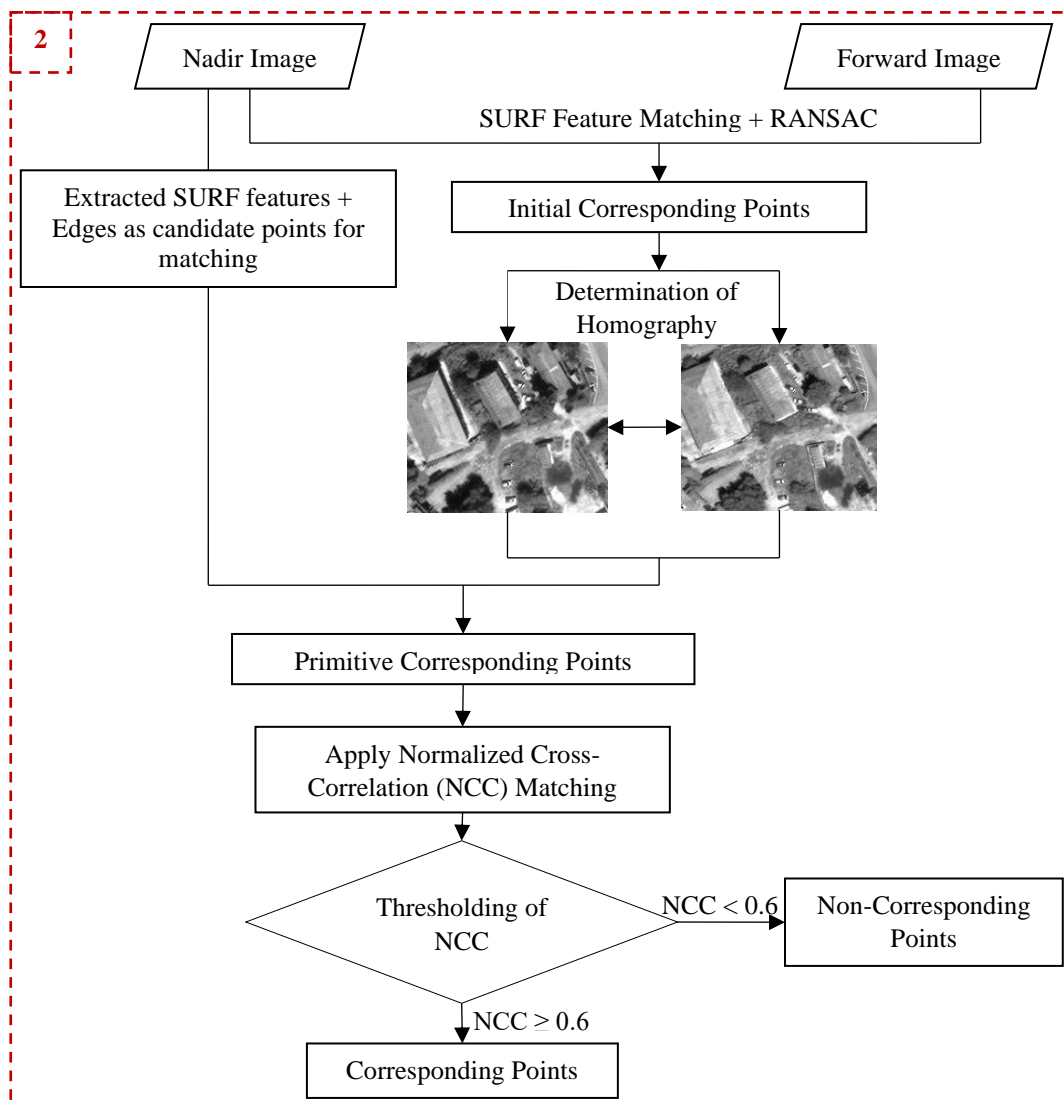Figure 2: Flowchart of the main steps for DSM Generation

Figure 3: Flowchart of the proposed method used for finding matching point.

At first we rely on the Speeded-Up Robust Features (SURF) (Banerjee & Mistry, 2017) algorithm to obtain the initial corresponding points after removing the incorrect matches by applying the widely used random sample consensus (RANSAC) algorithm available in the MATLAB. Next, the input images are partitioned into smaller localized regions. It is based on the hypothesis that the scene within those localized regions is planar and the images of 3D points lying on this plane are related to each other in different views by a planar homography (Chen et al., 2008). That is, for points sharing a plane in 3D scene, image projections from one view to another can be constructed by a homography as shown in Equation (1).

$$x^{'} = Hx \tag{1}$$

where x and x' are element by element homogeneous coordinates in two views of a same scene, while H is a 3 by 3 homography matrix. Given at least four reliable sets of point correspondence present within the regions, the singular value decomposition (SVD) technique (Klema & Laub, 1980) can be applied for computing the 3 by 3 homography matrix for each partitioned image. In the first matching stage, all matching primitives lying within these localized regions in image one (Nadir) are then transferred by using homography to image two (Forward) as their corresponding matching hypothesis. In our study, two types of matching primitives are applied. One includes all SURF points detected excluding initial corresponding points used for computing homography, and the other is the edges detected of objects in an image using canny edge detection (Xu et al., 2017).

In the second matching stage, for any correspondence matching hypothesis obtained through planar homography, they are further matched using normalized cross-correlation coefficient similarity constraint. Firstly, for reference point e (see Figure 4) with its corresponding matching candidate denoted as e' in the search image, we define the searching window (15 x 15 pixel^2) as a square with a center at point e'. All pixels in this searching window are regarded as possible matching candidates. Secondly, a template window (12 x 12 pixel^2) moves pixel by pixel over the search window and a correlation coefficient is calculated in each position. The position where the correlation coefficient reaches its highest value is selected as a position of the best match. In the process, a method of thresholding is applied for eliminating the outliers. For example, a threshold value of 0.6 was used in our study. However, in general setting a threshold for a correlation coefficient may not always eliminate all the mismatches. For example, when working with natural targets some good matches may be excluded while some mismatches remain. Therefore, in our experiment the sequenced wrong correspondence is removed further based on location property (pixel distance) of the feature points such that they fulfill two conditions: Firstly, the same numbers of points must lie within a buffer of certain radius (30 pixels in our case) in both the images. Secondly, the pixel distance between the center points to all other matched points in both images must not deviate more than 5 pixels. Finally, this procedure is applied for all the matching primitives in the region to obtain final matching points. Now all these dense point correspondences generated through image matching were used to determine the three-dimensional coordinates by employing the RPC model.
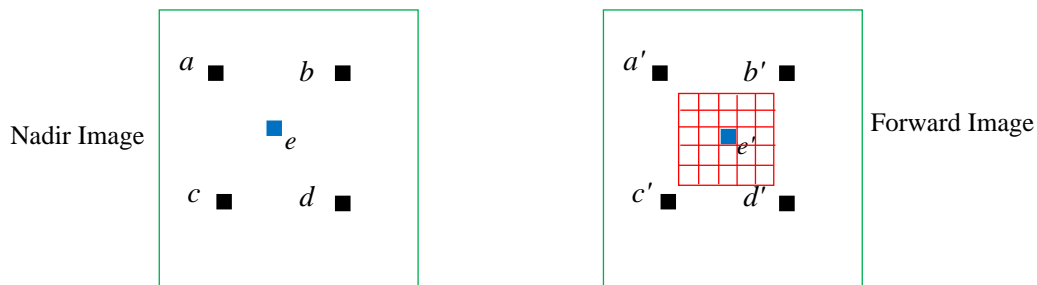

Figure 4: Four sets of initial point correspondences *(a, a'), (b, b'), (c, c'),* and *(d, d')* used for computing homography matrix and *(e, e')* is the matching primitives and its corresponding matching hypothesis.

3.2 Least-Square Solutions to the RPC Model

At this stage, the rational polynomials are fitted to the image coordinates and their corresponding object coordinates of the dense image points is estimated. The RPC model is a generalized high approximation accuracy sensor orientation model. The RPC model relates the ground coordinates to its corresponding image pixel coordinates using a ratio polynomial. It describes the relationship between 2D image coordinate and 3D object coordinate by rational polynomial using 80 coefficients (RPCs). It is characterized by a line l and sample s of the image pixel coordinates corresponding to the approximate ground coordinates (latitude φ, longitude λ and ellipsoidal height h) (Grodecki & Dial, 2003). The RPC model provides the relationships between image and object coordinates as follows:

$$l = l_s l_n + l^o \tag{2}$$

$$s = s_s s_n + s^o \tag{3}$$

$$l_n = \frac{Num_l(\phi_n, \lambda_n, h_n)}{Den_l(\phi_n, \lambda_n, h_n)} \tag{4}$$

$$s_n = \frac{Num_s(\phi_n, \lambda_n, h_n)}{Den_s(\phi_n, \lambda_n, h_n)} \tag{5}$$

$$Num_l(\phi_n, \lambda_n, h_n) = a_1 + a_2\lambda_n + a_3\phi_n + a_4 h_n + a_5\lambda_n\phi_n + a_6\lambda_n h_n + a_7\phi_n h_n + a_8\lambda_n^2 + a_9\phi_n^2 + a_{10}h_n^2 + a_{11}\lambda_n\phi_n h_n + a_{12}\lambda_n^2\phi_n + a_{13}\lambda_n^2 h_n$$
$$+ a_{14}\lambda_n\phi_n^2 + a_{15}\phi_n^2 h_n + a_{16}\lambda_n h_n^2 + a_{17}\phi_n h_n^2 + a_{18}\lambda_n^3 + a_{19}\phi_n^3 + a_{20}h_n^3 \tag{6}$$

$$Den_l(\phi_n, \lambda_n, h_n) = b_1 + b_2\lambda_n + b_3\phi_n + b_4 h_n + ... + b_{20}h_n^3 \tag{7}$$

$$Num_s(\phi_n, \lambda_n, h_n) = c_1 + c_2\lambda_n + c_3\phi_n + c_4 h_n + ... + c_{20}h_n^3 \tag{8}$$

$$Den_s(\phi_n, \lambda_n, h_n) = d_1 + d_2\lambda_n + d_3\phi_n + d_4 h_n + ... + d_{20}h_n^3 \tag{9}$$

Here, (l_n, s_n) are the normalized (offset and scaled) image coordinates estimated from the measured line and sample coordinates; whereas (ϕ_n, λ_n, h_n) are the corresponding object point coordinates in terms of normalized latitude ϕ, longitude λ and ellipsoidal height h given by:

$$\phi_n = \frac{\phi - \phi_o}{\phi_s}; \ \lambda_n = \frac{\lambda - \lambda_o}{\lambda_s}; \ h_n = \frac{h - h_o}{h_o} \tag{10}$$

In order to remove the unacceptable residual biases in the image coordinates, we introduce bias parameters by incorporating translation parameters (A_0 and B_0) and modify Equations (2) and (3) as:

$$l + A_0 = l_s \frac{Num_l(\phi_n, \lambda_n, h_n)}{Den_l(\phi_n, \lambda_n, h_n)} + l^o \tag{11}$$

$$s + B_0 = s_s \frac{Num_s(\phi_n, \lambda_n, h_n)}{Den_s(\phi_n, \lambda_n, h_n)} + s^o \tag{12}$$

RPC model is a non-linear polynomial function, Equations (11) and (12) can be written using first order Taylor's series approximation as:

$$\begin{pmatrix} l \\ s \end{pmatrix} = \begin{pmatrix} l_o \\ s_o \end{pmatrix} + \begin{pmatrix} l_s \frac{\partial l}{\partial \phi} & l_s \frac{\partial l}{\partial \lambda} & l_s \frac{\partial l}{\partial h} \\ s_s \frac{\partial s}{\partial \phi} & s_s \frac{\partial s}{\partial \lambda} & s_s \frac{\partial s}{\partial h} \end{pmatrix} \begin{pmatrix} \delta\phi \\ \delta\lambda \\ \delta h \end{pmatrix} \tag{13}$$

Here, l_o and s_o denote, the line and sample respectively of image coordinates, corresponding to the initial approximate ground coordinates.

Now, the 4 residual equations for Nadir (N) and Forward (F) images will be expressed as Equation (14) and solve for unknowns iteratively via least square method.

$$\underbrace{\begin{pmatrix} V_{N,l} \\ V_{N,s} \\ V_{F,l} \\ V_{F,s} \end{pmatrix}}_{V_{all}} = \underbrace{\begin{pmatrix} l_s \frac{\partial l_N}{\partial \phi} & l_s \frac{\partial l_N}{\partial \lambda} & l_s \frac{\partial l_N}{\partial h} \\ s_s \frac{\partial s_N}{\partial \phi} & s_s \frac{\partial s_N}{\partial \lambda} & s_s \frac{\partial s_N}{\partial h} \\ l_s \frac{\partial l_F}{\partial \phi} & l_s \frac{\partial l_F}{\partial \lambda} & l_s \frac{\partial l_F}{\partial h} \\ s_s \frac{\partial s_F}{\partial \phi} & s_s \frac{\partial s_F}{\partial \lambda} & s_s \frac{\partial s_F}{\partial h} \end{pmatrix}}_{A_{all}} \underbrace{\begin{pmatrix} \delta\phi \\ \delta\lambda \\ \delta h \end{pmatrix}}_{\Delta} + \underbrace{\begin{pmatrix} l_{o,N} \\ s_{o,N} \\ l_{o,F} \\ s_{o,F} \end{pmatrix} - \begin{pmatrix} l_N \\ s_N \\ l_F \\ s_F \end{pmatrix} - \begin{pmatrix} A_{o,N} \\ B_{o,N} \\ A_{o,F} \\ B_{o,F} \end{pmatrix}}_{B_{all}}; \ V_{all} = A_{all}\Delta + B_{all} \ ; \Delta = -\left(A_{all}^T A_{all}\right)^{-1}\left(A_{all}^T B_{all}\right); \begin{pmatrix} \phi = \phi_o + \delta\phi \\ \lambda = \lambda_o + \delta\lambda \\ h = h_o + \delta h \end{pmatrix} \tag{14}$$

3.3 Spatial Interpolation Methods

The result of image matching followed by iterative least squares adjustment using 4 residual equations to derive object space coordinates in Geographic coordinates in WGS84 datum is a set of 3D points representing the earth surface (top of everything). Finally, all sets of irregular 3D tie-points generated thereafter were then utilized as an input to each of the interpolation methods for establishing the three dimensional coordinates for the entire terrain on a regularly spaced grid of resulting DSM. The raster data model is built from the spot elevations to estimate the elevation at each grid cell. Inverse Distance Weighted (IDW) and Kriging interpolation techniques have been used in this study. The IWD gives a weighted average interpolated value using the nearest reference points within a defined neighborhood around each grid cell (Arun, 2013; Caruso & Quarta, 1998; Habib et al., 2020). In Ordinary Kriging, the prediction at an un-sampled point is a weighted linear combination of all already observed points modelled under the assumption that the process is second-order stationary (Ryu et al., 2002; Van Beers & Kleijnen, 2004).

4. RESULTS

4.1 Image Matching

The matching procedure described earlier yields a reasonable number of good matching points. In order to access the matching performance of our method, we use the same set of feature correspondences detected by SURF earlier as reference points in our matching procedure. Figure 5 shows that RMSEs in line and sample of the matching results obtained by correlation coefficient in conjunction with homography for the same initial correspondence points. Figure 6 shows an increased matching tie-points after final matching propagation for the specific region of the tested stereo images.
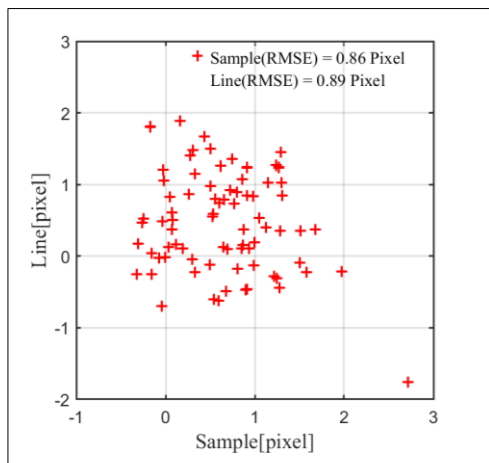

Figure 5: Scattergram of errors of matching image coordinates and its RMSEs.

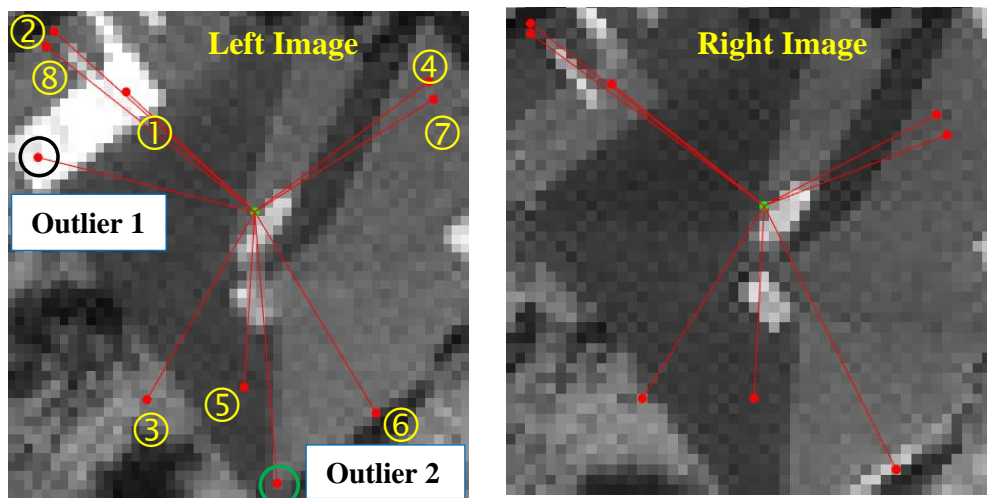Figure 6: Final tie points generated for the specific region of the tested image.

Figure 7: Figure showing the distribution of matching points within a buffer for outlier detection and removal.

4.2 Result of Coordinates Estimation using RPC Model

The locations of GCPs are shown in Figure 8. Estimates of the ground coordinates (elevation) for the 49 checkpoints are shown in Table 2. The fourth column represents absolute deviation of the elevation (in meters) from their observed values. Table 2 shows that maximum absolute deviation of the height from the check set is equal to 4.709 m. The absolute values of the relative error are presented in the last column. Additionally, the RMSEs of easting, northing and height for the coordinates estimated from stereo images were 2.90 m, 2.92 m and 1.64 m respectively.

$$\Delta H_i = |H_i' - H_i| \; ; \; \varepsilon_H(i) = |\frac{H_i' - H_i}{H_i}| \; ; \; RMSE = \sqrt{\frac{1}{N}\sum_{i=1}^{n}(\Delta H_i)^2} \tag{15}$$

(a)   (b)
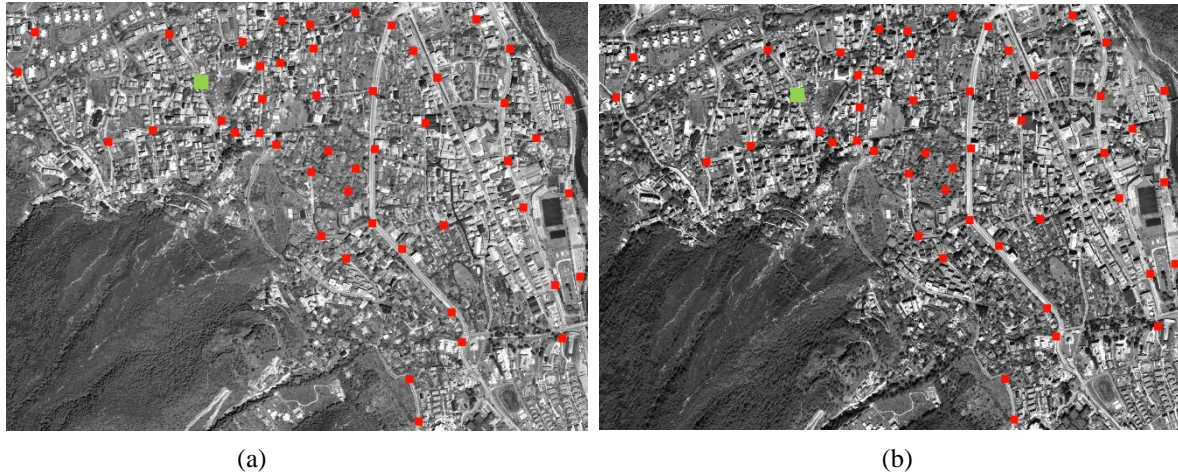
Figure 8: Distribution of the known GCPs over the stereo satellite image: (a) Nadir image (b) Forward image. Red squares show the check GCPs and green square show the GCP used for bias-correction.

Table 2: Deviation of the ground height from check GCP set

Check GCP	Ellipsoidal heights in meter				Check GCP	Ellipsoidal heights in meter			
	Estimated (H')	Observed (H)	ΔH	ε_H		Estimated (H')	Observed (H)	ΔH	ε_H
1	2322.12	2322.52	0.403	0.017	26	2333.50	2332.04	1.465	0.063
2	2309.32	2306.19	3.129	0.136	27	2346.07	2344.93	1.143	0.049
3	2289.99	2290.32	0.337	0.015	28	2372.34	2369.72	2.617	0.110
4	2280.45	2279.39	1.062	0.047	29	2380.17	2377.19	2.981	0.125
5	2281.95	2281.37	0.579	0.025	30	2392.91	2389.08	3.825	0.160
6	2281.44	2280.48	0.960	0.042	31	2397.86	2398.60	0.738	0.031
7	2271.09	2271.65	0.554	0.024	32	2431.48	2430.98	0.493	0.020
8	2268.00	2268.33	0.334	0.015	33	2461.14	2456.43	4.709	0.192
9	2266.39	2265.81	0.585	0.026	34	2419.49	2420.14	0.652	0.027
10	2266.48	2265.52	0.960	0.042	35	2414.28	2411.06	3.221	0.134
11	2277.26	2275.43	1.831	0.080	36	2387.65	2388.70	1.053	0.044
12	2325.93	2325.90	0.033	0.001	37	2380.88	2381.71	0.833	0.035
13	2302.19	2303.30	1.114	0.048	38	2379.43	2379.58	0.152	0.006
14	2325.11	2324.11	0.999	0.043	39	2369.96	2370.79	0.835	0.035
15	2328.92	2326.93	1.995	0.086	40	2357.73	2356.15	1.586	0.067
16	2312.09	2313.31	1.217	0.053	41	2371.74	2368.99	2.758	0.116
17	2319.00	2317.59	1.407	0.061	42	2358.21	2356.96	1.250	0.053
18	2324.64	2323.86	0.776	0.033	43	2356.64	2356.64	0.002	0.000
19	2278.79	2278.00	0.793	0.035	44	2335.90	2337.32	1.421	0.061
20	2321.69	2321.70	0.011	0.000	45	2359.78	2357.74	2.038	0.086
21	2327.47	2329.61	2.134	0.092	46	2354.47	2352.66	1.812	0.077
22	2344.34	2343.90	0.436	0.019	47	2279.06	2277.70	1.361	0.060
23	2343.23	2341.58	1.654	0.071	48	2486.83	2488.59	1.759	0.071
24	2329.67	2330.22	0.555	0.024	49	2479.69	2479.27	0.421	0.017
25	2346.71	2347.45	0.744	0.032					

4.3 Spatial Interpolation

In order to implement the interpolation as a prediction criterion, a curtailment procedure is applied to curtail some values from the original block of values for the purpose of predicting them later. In our experiment 10% of the original values are curtailed and used as check points (CPs). The validation of the interpolated results was carried out based on relevant descriptive statistics such as: the minimum and maximum error, mean absolute error (*MAE*), root-mean-square error (*RMSE*), and sample standard deviation (*StDev*) as indicated in Equations (15), (16) and (17).

$$MAE = \frac{1}{N} \sum_{i=1}^{n} |\Delta H_{(i)}| \tag{16}$$

$$StDev = \sqrt{\frac{1}{N-1} \sum_{i=1}^{n} (H_{(i)} - H_{mean})^2} \tag{17}$$

where N is the checkpoints number and H_{mean} is the mean value of the measured elevations. *MAE* is a measure of how far 'off' a measurement is from extracted value, *RMSE* is a measures of goodness of fit and *StDev* is a measure of the amount of variation. Figure 9 shows the histograms of the elevation errors and the regression model fit derived from the IDW, and Kriging predictors. Figure 10 show the DSM surfaces built by IDW and Kriging interpolation methods with a cell size of 2 m.
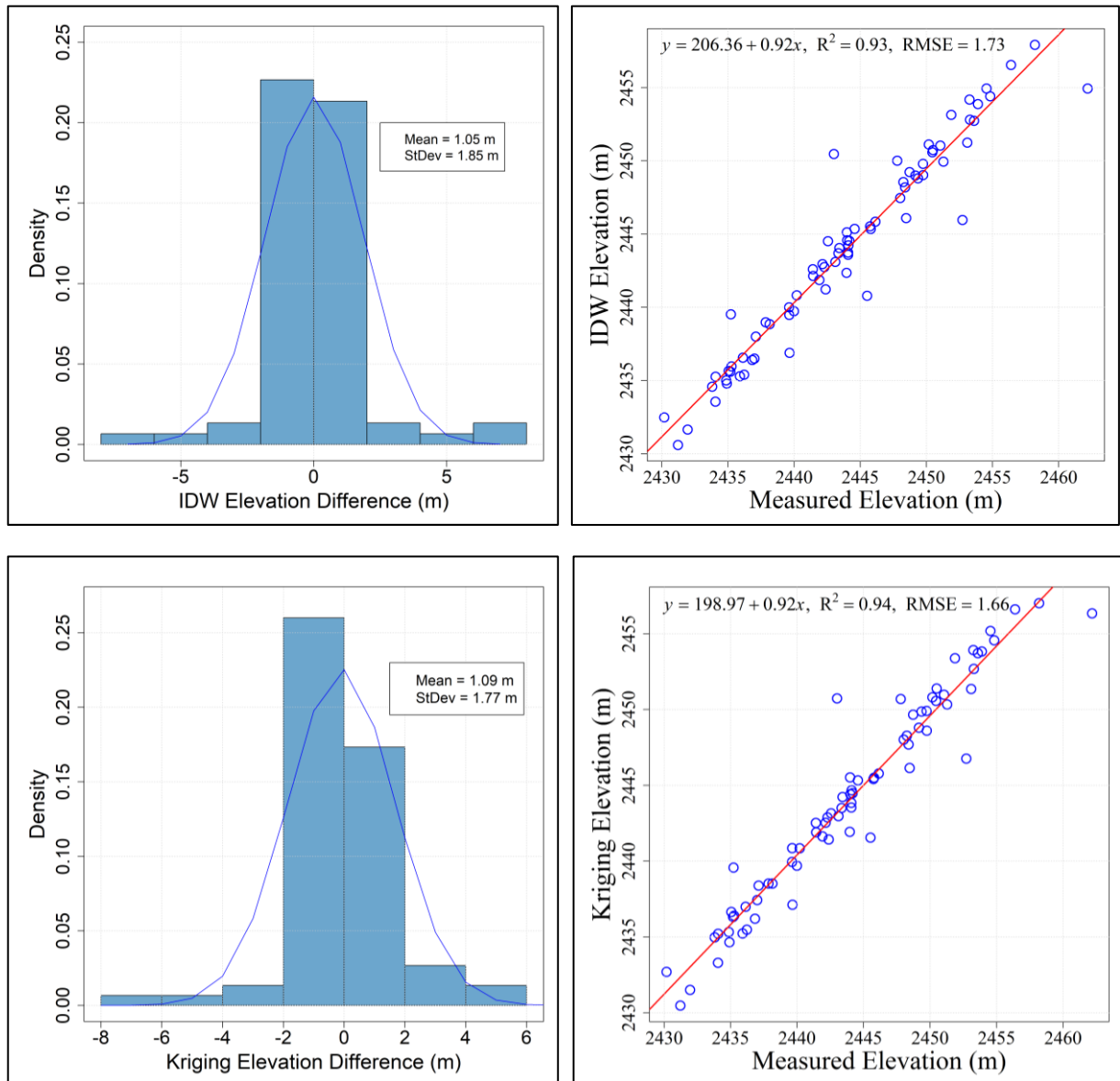

Figure 9: Histogram graph of elevation differences, relevant descriptive statistics, and regression model of measured elevations versus interpolated values.

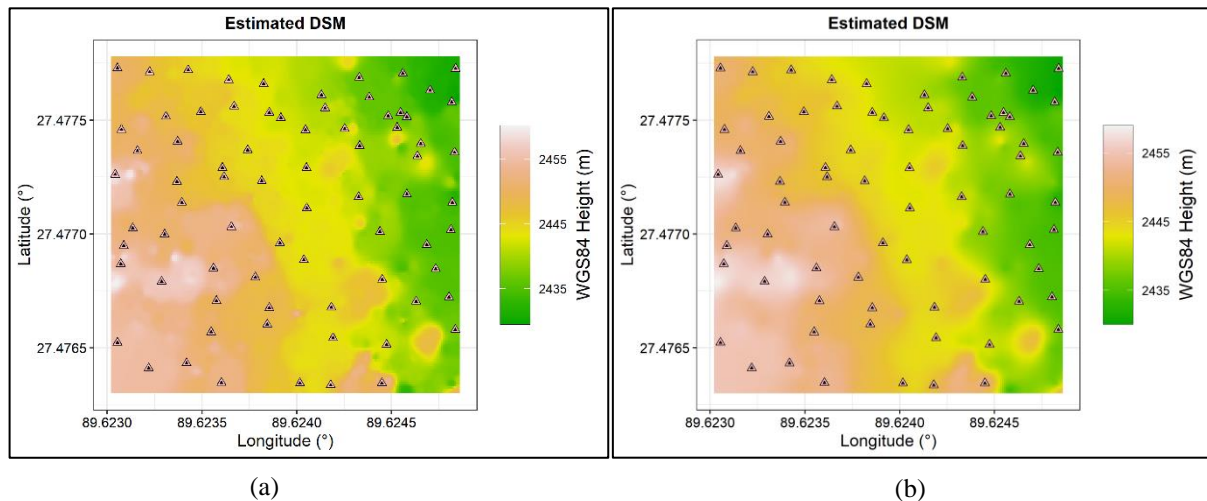| | (a) | | (b) |

Figure 10: (a) DSM surface generated by the IDW interpolator method and (b) DSM surface generated by the Kriging interpolator method with locations of CPs.

5. DISCUSSION

The result of the ground coordinates estimated using bias-compensated RPCs from WV-3 data evaluated over the 49 GCPs as shown in Table 2 highlight that the proposed method is simple and effective in estimating 3D coordinates at points of interest that have the potential to generate such explicit image-based 3D information. We also examined the effectiveness of different GCPs during the bias-compensation process. The only one reliable GCP is used for bias-compensation as shown in Figure 8. In our experiment, we found that GCPs located relatively on flat ground with sharply-definable ground points increased the expected accuracy of estimated ground coordinates.

In DSM generation it is well known that image matching is the critical issue within the considered images. The RMSEs in line and sample of the matching results shown in Figure 5 obtained by correlation coefficient in conjunction with homography used in our study is a simple method to stabilize stereo correspondence computation. Moreover, in our method the use of the image distance property of a feature point to effectively identify isolated points as outliers demonstrated its ability to remove significant number of wrong correspondences in generating reliable sets of tie points.

The visualization of geospatial entities generally entails DSMs/DEMs that are interpolated to establish 3D coordinates for the entire terrain within the study area. The study evaluated the performance of IDW and Kriging interpolated surfaces using the spatial data estimated via RPC model. The results presented in Figure 9 indicate the consistency between the statistical parameters of IDW and Kriging algorithms such as MAE, StDev and RMSE. Furthermore, concerning the DSMs generation, the main and still open problem is obviously the dense matching strategy, in order to reach a better reconstruction of the texture of buildings in the scene, presently not sufficiently delineated as shown in Figure 10. The further optimization of the matching algorithm parameters would likely improve the result.

6. CONCLUSION AND FUTURE RESEARCH

The topographical information is some essential geo-spatial datasets for various surveying and engineering applications. An elevation model is the continuous 3D depiction of the Earth's surface that is produced through many techniques such as remote sensing, photogrammetry and land surveying. In fact, very-high resolution satellite sensors allow the acquisition of spatial data directly which are equivalent to DSM. This study evaluated the accuracy of a DSM generated by processing Ortho-Ready Standard imagery from WV-3 using supplied RPCs. The use of a bias-compensated RPC model with two shift parameters showed that the easting, northing and height errors of the coordinates estimated were 2.90 m, 2.92 m and 1.64 m respectively. The results were well consistent with the expected accuracy of Ortho-Ready Standard imagery satisfying the target accuracy of approximately 4 m as specified under DigitalGlobe Core Imagery Product Guide of WV-3.

Concerning DSMs generation, generating dense tie points is a critical step that enables its quality. We rely on homography transformation stereo matching in conjunction with normalized cross-correlation coefficient matching constraints. Additionally, we presented the property of image pixel distance to effectively identify and remove isolated outliers as non-matching tie points from the images.

Furthermore, visual comparisons of interpolated surfaces between IDW and Kriging interpolators have also been presented in this paper. Investigations revealed that both Kriging and IDW methods have been found to perform better in geo-morphologically smooth areas than in urban areas which might be attributed to not having sufficient matching tie points. In future we aim to optimize the matching algorithm parameters which are likely to improve the results, as well as the possible integration of the concept of semi-global matching.

In future research, this technique can be explored in time-series satellite images to analyze the suitability and its performance in giving a synthesis of detecting, analyzing and updating the dynamics of various points of interest in 3-Dimension. Moreover, with this three dimensional information, the scope can be extended to applications requiring vertical information such as monitoring the growth of urban areas, detecting collapsed buildings, and tree growth which 2D analysis mainly ignores. This might be achieved by a simple subtraction of multi-temporal DSMs, resulting in a reasonable approximation of height residual to indicate potential changes.

REFERENCES

Arun, P. V., 2013. A comparative analysis of different DEM interpolation methods. Egyptian Journal of Remote Sensing and Space Science, 16(2), 133–139.

Banerjee, A., and Mistry, D., 2017. Comparison of Feature Detection and Matching Approaches: SIFT and SURF. GRD Journals-Global Research and Development Journal for Engineering, 2(March), 7–13.

Caruso, C., and Quarta, F., 1998. Interpolation methods comparison. Computers and Mathematics with Applications, 35(12), 109–126.

Chen, C. I., Sargent, D., Tsai, C. M., Wang, Y. F., and Koppel, D., 2008. Stabilizing stereo correspondence computation using delaunay triangulation and planar homography. Lecture Notes in Computer Science (Including Subseries Lecture Notes in Artificial Intelligence and Lecture Notes in Bioinformatics), 5358 LNCS(PART 1), 836–845.

Fratarcangeli, F., Murchio, G., Di Rita, M., Nascetti, A., and Capaldo, P., 2016. Digital surface models from ZiYuan-3 triplet: performance evaluation and accuracy assessment. International Journal of Remote Sensing, 37(15), 3505–3531.

Grodecki, J., and Dial, G., 2003. Block adjustment of high-resolution satellite images described by Rational Polynomials. Photogrammetric Engineering and Remote Sensing, 69(1), 59–68.

Habib, M., Alzubi, Y., Malkawi, A., and Awwad, M., 2020. Impact of interpolation techniques on the accuracy of large-scale digital elevation model. Open Geosciences, 12(1), 190–202.

Hengl, T., and Reuter, H., 2011. How accurate and usable is GDEM? A statistical assessment of GDEM using LiDAR data. Handbook of Quantitative and Theoretical Geography or Advances in Quantitative and Theoretical Geography, July, 000–046.

Klema, V. C., and Laub, A. J., 1980. The Singular Value Decomposition: Its Computation and Some Applications. IEEE Transactions on Automatic Control, 25(2), 164–176.

Rodríguez, E., Morris, C. S., and Belz, J. E., 2006. A global assessment of the SRTM performance. Photogrammetric Engineering and Remote Sensing, 72(3), 249–260.

Ryu, J. S., Kim, M. S., Cha, K. J., Lee, T. H., and Choi, D. H., 2002. Kriging interpolation methods in geostatistics and DACE model. KSME International Journal, 16(5), 619–632.

Štular, B., Lozić, E., and Eichert, S., 2021. Airborne LiDAR-derived digital elevation model for archaeology. Remote Sensing, 13(9).

Susaki, J., and Kishimoto, H., 2015. Improving the accuracy of estimated 3D positions using multi-temporal ALOS/prism triplet images. ISPRS Annals of the Photogrammetry, Remote Sensing and Spatial Information Sciences, 2(3W4), 223–230.

Takaku, J., Tadono, T., and Tsutsui, K., 2014. Generation of high resolution global DSM from ALOS PRISM. International Archives of the Photogrammetry, Remote Sensing and Spatial Information Sciences - ISPRS Archives, 40(4), 243–248.

Van Beers, W. C. M., and Kleijnen, J. P. C., 2004. Kriging interpolation in simulation: A survey. Proceedings - Winter Simulation Conference, 1, 113–120.

Wang, J., Zhang, N., Wu, X., and Wang, W., 2020. Hierarchical point matching method based on triangulation constraint and propagation. ISPRS International Journal of Geo-Information, 9(6).

Xu, Z., Baojie, X., and Guoxin, W., 2017. Canny edge detection based on Open CV. ICEMI 2017 - Proceedings of IEEE 13th International Conference on Electronic Measurement and Instruments, 2018-January(1), 53–56.